Characterization of Mechanical and Optical Properties of X-Ray Mask Membranes

RLE Technical Report No. 564

Flora S. Tsai

June 1991

Research Laboratory of Electronics
Massachusetts Institute of Technology
Cambridge, Massachusetts 02139-4307

This work was supported in part by the National Science Foundation under Grant ECS 90-16437 and in part by the Naval Research Laboratory under Contract N00014-90-K-2018.

Characterization of Mechanical and Optical Properties Of X-Ray Mask Membranes

by

Flora S. Tsai

Submitted to the Department of Electrical Engineering and Computer Science

May 1991

in Partial Fulfillment of the Requirements for the Degree of

Bachelor of Science in Electrical Engineering

ABSTRACT

X-ray mask technology is of primary importance in the implementation of x-ray lithography in the manufacturing process. Essential to the production of a viable x-ray mask is the development of strong, high-quality mask membranes. The membrane material should have a very flat surface, high strength, high optical and x-ray transparency, and low susceptibility radiation damage. This thesis focuses on the comparative study of the mechanical and optical characteristics of x-ray mask membranes of two different electronic materials, silicon nitride and poly-silicon. Membranes were analyzed for uniformity in stress, Young's modulus, burst strength, optical transparency, thickness, index of refraction, and light scattering. In particular, this thesis describes a new optical transmission experiment allowing for the unambiguous determination of thickness as well as the real and imaginary components of the refractive index.

Thesis Supervisor: Prof. Henry I. Smith

Title: Professor of Electrical Engineering and Computer Science

TABLE OF CONTENTS

LIST OF FIGURES

ACKNOWLEDGEMENT

I wish to thank my thesis advisor, Prof. Henry I. Smith, for his supervision and help throughout the course of my work. I am also grateful for the expertise and guidance of Dr. Mark Schattenburg and Yao-Ching Ku though various phases of the project. Their helpful advice and comments are sincerely appreciated.

This thesis could not have been completed without the support of Dr. George Celler and the X-Ray Lithography team at Bell Labs, who provided me with the opportunity to use my summer work as part of the thesis.

Thanks also goes to the members of the Submicron Structures Laboratory and the members of the Center for Space Research for their technical assistance and cooperation during the course of the project.

Lastly, I am indebted to my parents and friends, who have given me continued care and support throughout the years, and to Chee, for providing me with encouragement and advice.

1. INTRODUCTION

X-ray lithography has become an active area of research since its introduction in 1972.(8) The advantages of x-ray lithography (XRL) include resolution below 0.1 μm, low scattering, broad process latitude, and high throughput. The main disadvantages are the high initial investment required for a synchrotron source as well as the integration of all the lithographic components into a realizable technology. (12) Other sources, such as laser-produced plasma sources, are available for medium resolution and medium throughput production.

At the present time, optical lithography is still the primary method for fabricating devices. However, as more chip memory is needed, the minimum linewidth should decrease and chip area should increase. The main trend towards smaller linewidths and larger chip area is shown in Figure 1. (13) If and when the time comes when optical lithography is no longer feasible, then x-ray or another type of lithography will have to be implemented. Working devices have already been fabricated using synchrotron and other types of x-ray sources. Yet, we are still far from implementing x-ray lithography in industry.

A significant hindrance toward the adoption of XRL as a manufacturing standard has been the diversity in mask and absorber materials. Once a uniform, well-defined process is established, XRL should be well on its way to industrial practice. In the search for the best x-ray mask material, several factors should be considered. This paper will focus on the study of two highly-acceptable materials: silicon nitride and polysilicon. Many important elements will be considered in determining the advantages and disadvantages of the materials, including ease of optical alignment and robustness in handling.

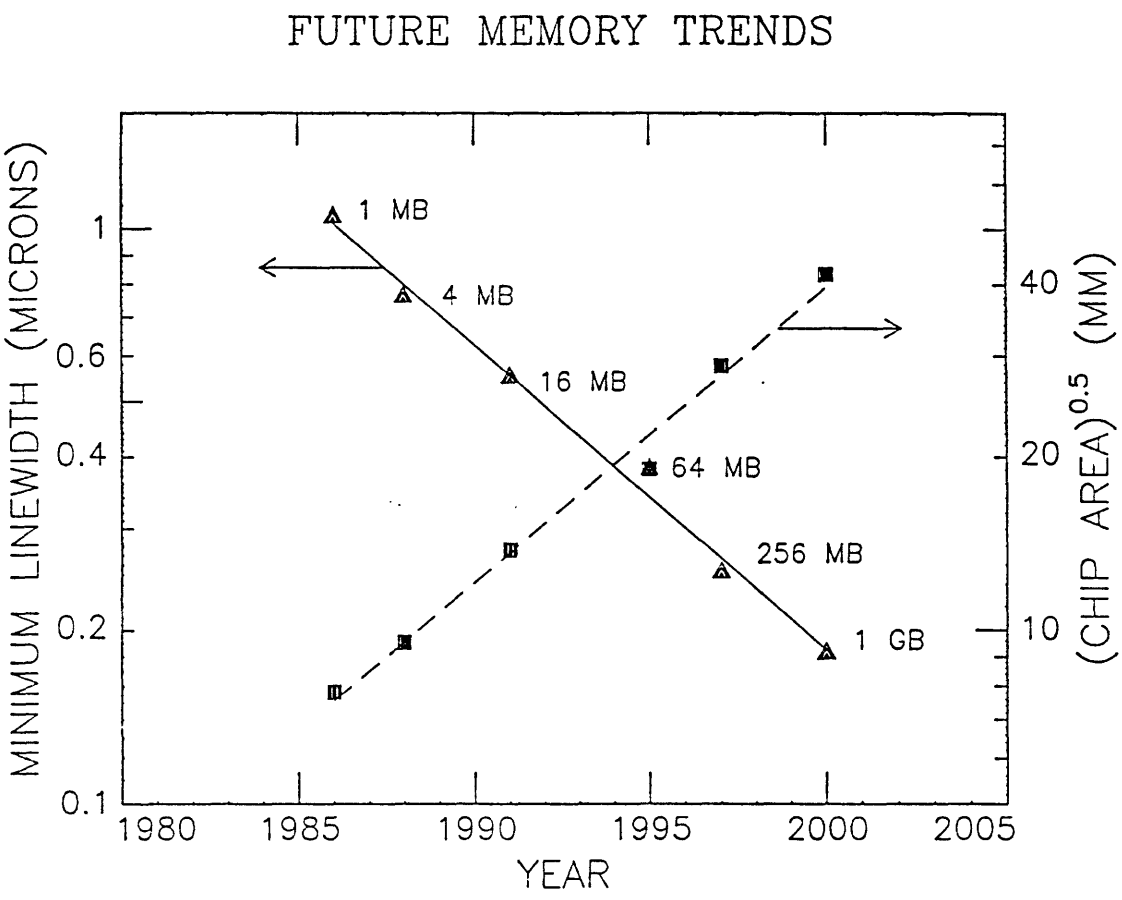

Figure 1. Trends towards smaller linewidths and larger area.

2. THEORY AND DESIGN

2.1 Background

An XRL system consists mainly of four components: a high power x-ray source, an x-ray mask, an x-ray sensitive resist material, and the exposure tool. The main problem lies in finding a good x-ray mask, which consists of an x-ray absorber pattern created on a thin x-ray transparent membrane supported by a rigid frame. The goal is to produce a thin but strong membrane that is transparent to x-rays. Among some of the many requirements for x-ray mask membranes are high Young's modulus, low tensile stress, high tensile strength, and good optical transparency. A good x-ray absorber material must have high absorption coefficient for x-ray absorption, steep profiles, good adhesion, and low stress. After selecting the proper mask substrate and absorber materials, the complete x-ray lithography mask structure must be mounted to a rigid ring of appropriate material, size, shape, and thickness to reduce distortions and allow for mask patterning. (5)

The x-ray lithographic technique is illustrated in Figure 2. The mask, which consists of an x-ray transparent membrane supporting a thin patterned film made of a material that strongly absorbs x-rays, is placed over a substrate coated with a radiation-sensitive resist. A distant "point" source of x-rays produced by a focused electron beam illuminates the mask, thus projecting the shadow of the x-ray absorber onto the polymer film. (2)

XRL uses contact / proximity printing with low-energy (1 - 2 keV) x-rays rather than optical radiation. By using x-rays, the diffraction problems common to photolithography are decreased, as well as the backscattering problem encountered in electron-beam lithography. Because of the x-ray's short wavelength (4-50 Å), there are no convenient mirrors or lenses

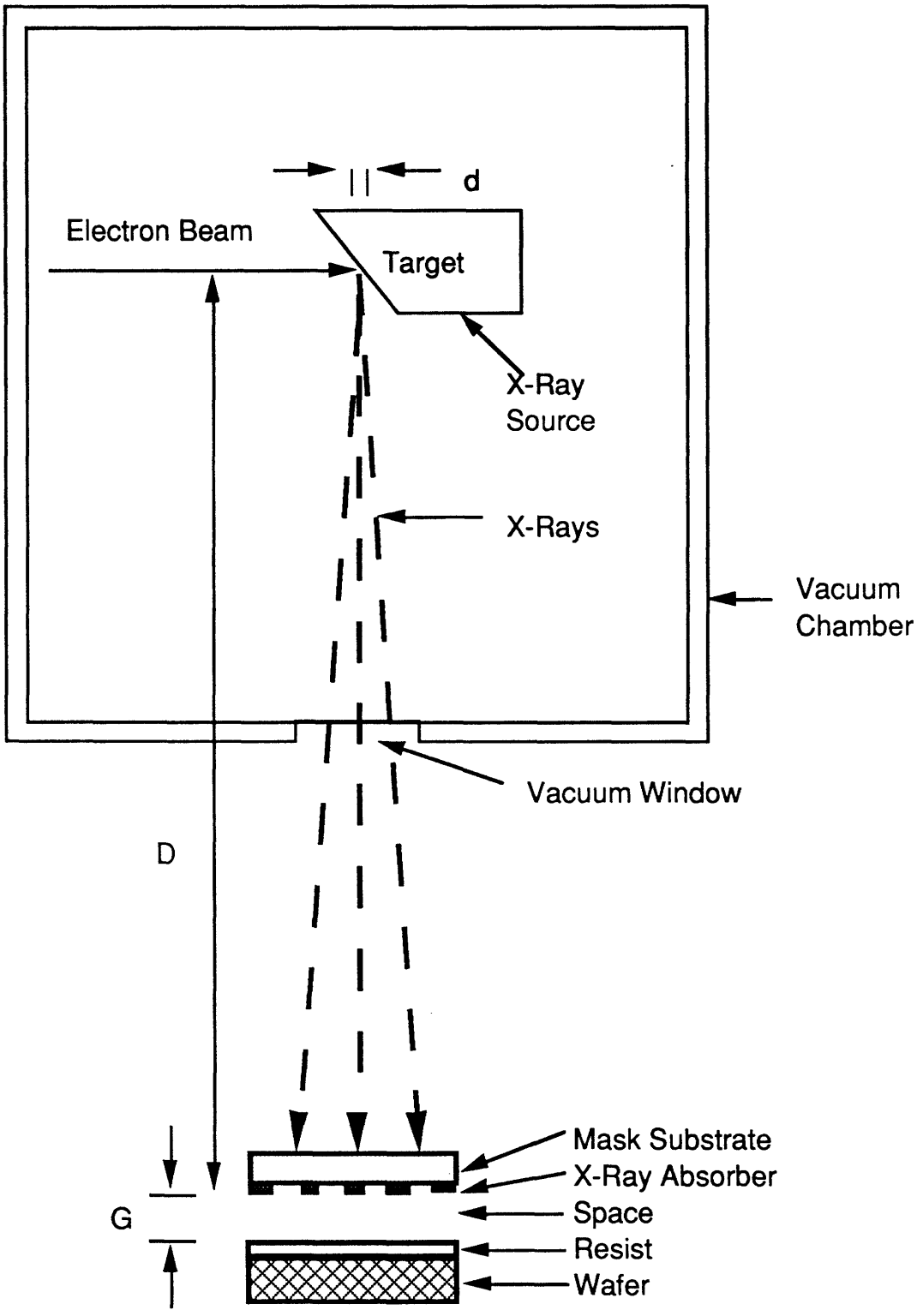

Figure 2. X-ray lithography technique.

that can be used to collimate the rays as in optical, uv, or electron-beam systems. Thus, an x-ray source of finite size has to be far enough away from the mask and resist for the x- ray to appear to arrive with small divergence. (2)

2.2 Theory

Both silicon nitride and polysilicon are well-suited materials for an x-ray mask membrane. Si-rich SiN_x membranes, if initially free of defects such as pinholes, are extremely strong and durable. For example, a 20 mm diameter, Si-rich SiN_x membrane, 1.4 μm thick, can sustain a full atmosphere of pressure differential, deflecting up to 700 μm without breaking. Such membranes do not break in ordinary usage unless struck directly with a sharply pointed object. They can be brought repeatedly into contact with a substrate, with no apparent damage.(3)

Polysilicon on silicate glasses are inexpensive and simple to fabricate. They are strong due to lack of cleave/slip planes, possess a high stiffness coefficient, yielding less distortion, and have relatively high optical transmittance.(9)

Other suitable materials for x-ray mask production are epi-Si, diamond, silicon carbide, and boron nitride. Epi-silicon, or single crystalline silicon, has good x-ray transparency at low energy, high Young's modulus, and is inexpensive to fabricate. Diamond is well-suited because of its high x-ray and optical transparency and high mechanical stiffness. Silicon carbide has good x-ray transparency at low energy, high optical transmittance, good distortion stability, and high Young's modulus. Boron nitride has good x-ray transparency at high energy, high optical transmittance, and high Young's modulus.

3. POLY-SI MEMBRANES ON SILICATE GLASSES

3.1 Formation of low temperature poly-Si membranes on silicate glasses

The following work with poly-Si membranes was done at AT&T Bell Laboratories in Murray Hill, NJ. Silicate glasses from Hoya Industries were found to have nominal thermal expansion coefficients of 3.7 $x10^{-6}$ $°C^{-1}$. Their anneal temperatures were specified as 680 °C. The 75 mm diameter, 0.4 mm thick glass substrates were first cleaned at 105 °C in sulfuric acid containing 5 % peroxide, followed by a 2 minute etch in 100:1 H_20/ 49% hydrofluoric acid (HF). One micron of LPCVD (low-pressure chemical vapor deposition) amorphous silicon was deposited on both sides of the wafers at 580 °C from silane decomposition at 200 mTorr. The silicon films were then annealed at temperatures between 580 °C and 680 °C to convert to polycrystalline silicon. (9)

Circular openings, 20 mm in diameter, were made in the poly-Si on one side of the wafers by reactive ion etching with NF_3 gas through a shadow mask to define the hole. The wafers were etched in a 5% HF solution, removing the glass in the defined openings. The poly-Si is virtually untouched by the HF, and thus becomes a membrane on the side opposite the opening, while acting as an etch mask to protect the other side. Etch rates in this solution were 60 μm/ hr at room temperature and 120 μm/ hr at 40 °C. (9)

The polycrystalline silicon membranes on fused silica were formed by the following steps: Nominally 1 μm thick LPCVD poly-Si layer was deposited by silane decomposition at 630 °C and 300 mTorr onto both sides of 3 in. diameter fused silica wafers with a peak-to-valley roughness <50 Å, obtained from Hoya Industries, Inc. A lithographic technique was then used to open a centered, 14 mm diameter poly-Si membrane on the other side of the wafer. Total etch times were 7 hr at room temperature and 2 hr if etchant was heated to 60 °C. (10)

3.2 Characterization of membranes

The quality of the membranes was then evaluated by different types of experimental measurements. A novel light scattering setup was used to evaluate the optical properties of the x-ray mask substrates. The stress and elastic modulus were measured by applying differential pressure to the membrane, also known as the "bulge" test. The thickness was calculated by determining the interference peaks obtained from the optical transmission measurements.

3.2.1 Light Scattering Setup (AT&T)

Figure 3 illustrates the basic light scattering experimental setup. The system discriminates between the forwardly transmitted and specularly reflected light from the sample membranes by use of perforated solid state light detectors. Both the back scattering and forward scattering detectors (FS) consist of commercially available solar cells. The detectors are placed on each side of the membrane to obtain simultaneous light measurements of forward and back scattering without being affected by thin film interference effects. In addition, both detectors are calibrated to the reference input light beam. The 633 nm light beam from a He-Ne laser is transmitted through the hole in the back scattering detector (BD). The specularly reflected light from the membrane is transmitted through the hole in the BD, and does not contribute to the scattered light signal. The forwardly transmitted light from the membrane is similarly directed through the hole in the FD, and it does not contribute to the forward scattering signal. In this fashion, the detectors collect only light that is back or forward scattered from the sample. Measurements can be made as a function of numerical aperture by means of the variable apertures located in front of each detector. (11)

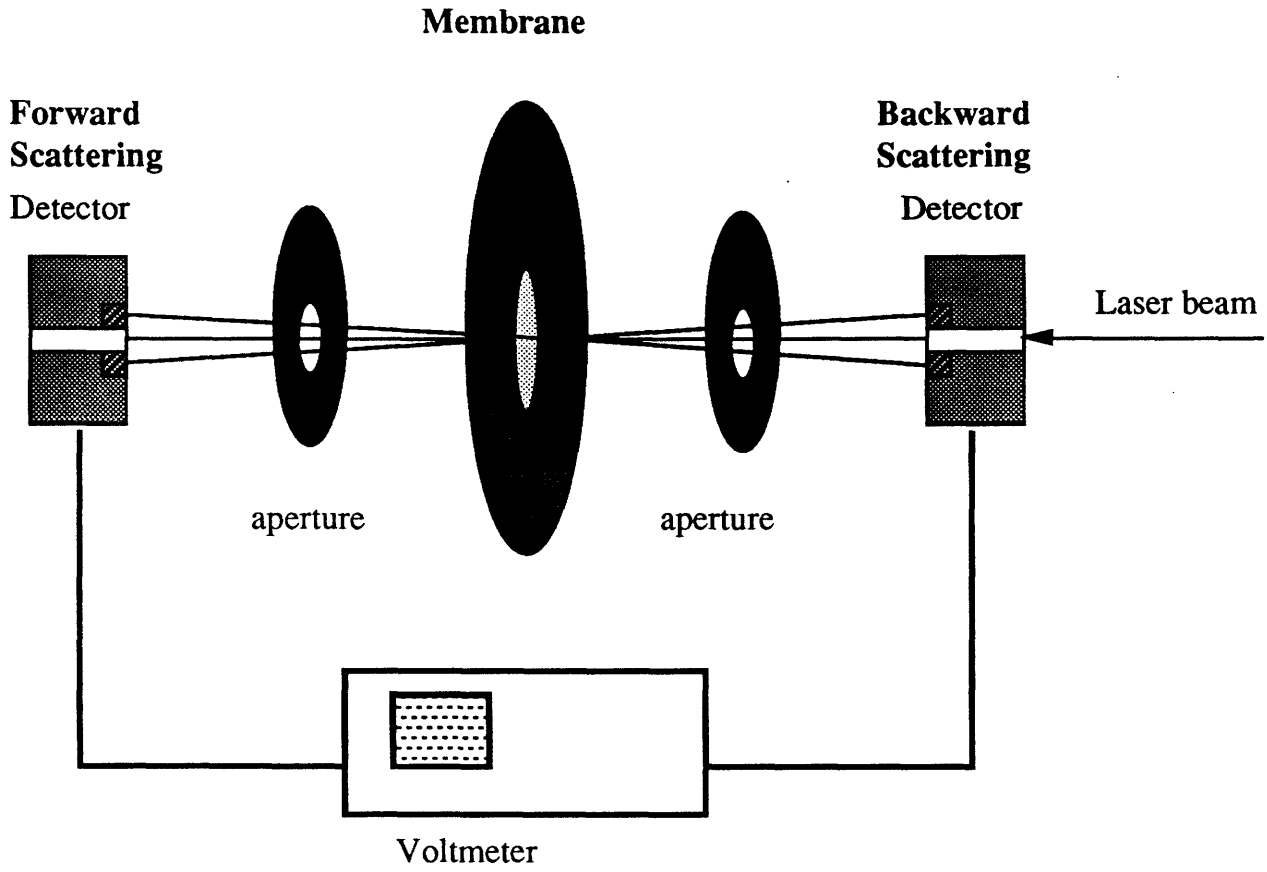

Figure 3. Light scattering diagram.

3.2.2 Stress Measurements (Bulge Test done at AT&T)

The relationship between the differential pressure P and membrane deflection h as determined by J. W. Beams is

$$P = \frac{4th}{r^2}\left(\sigma_o + \frac{2}{3}\frac{E}{1-\nu}\frac{h^2}{r^2}\right)$$

in which t is the membrane thickness, r is the radius of the membrane opening in the wafer, σ_o is the residual stress in the membrane (zero pressure differential), and E/ 1-v is the bulk modulus of elasticity. The membrane deflection h is the bulge height of the membrane at its center due to the differential pressure. This value is determined from the deflection of a laser beam reflected from the membrane surface. Refer to Figure 4 for schematic.(10)

An Automatic Radius of Curvature (AROC) machine was used for making the stress measurements. The method used to control the differential pressure across the membrane is depicted schematically in Figure 5. The mask was held in place with a double o-ring seal. An MKS 250B controller was used to regulate the flow of nitrogen to the back side of the mask through a 100 ccm MKS 248 flow valve. Pressure was monitored with an MKS 220, 0-1 torr capacitance manometer. Typical variation in the pressure was $\pm$ 0.010 torr.

In order to measure the resultant bow after pressurizing the membrane, an AROC system was used. A He-Ne laser was focused on the membrane. The reflected laser signal was bounced

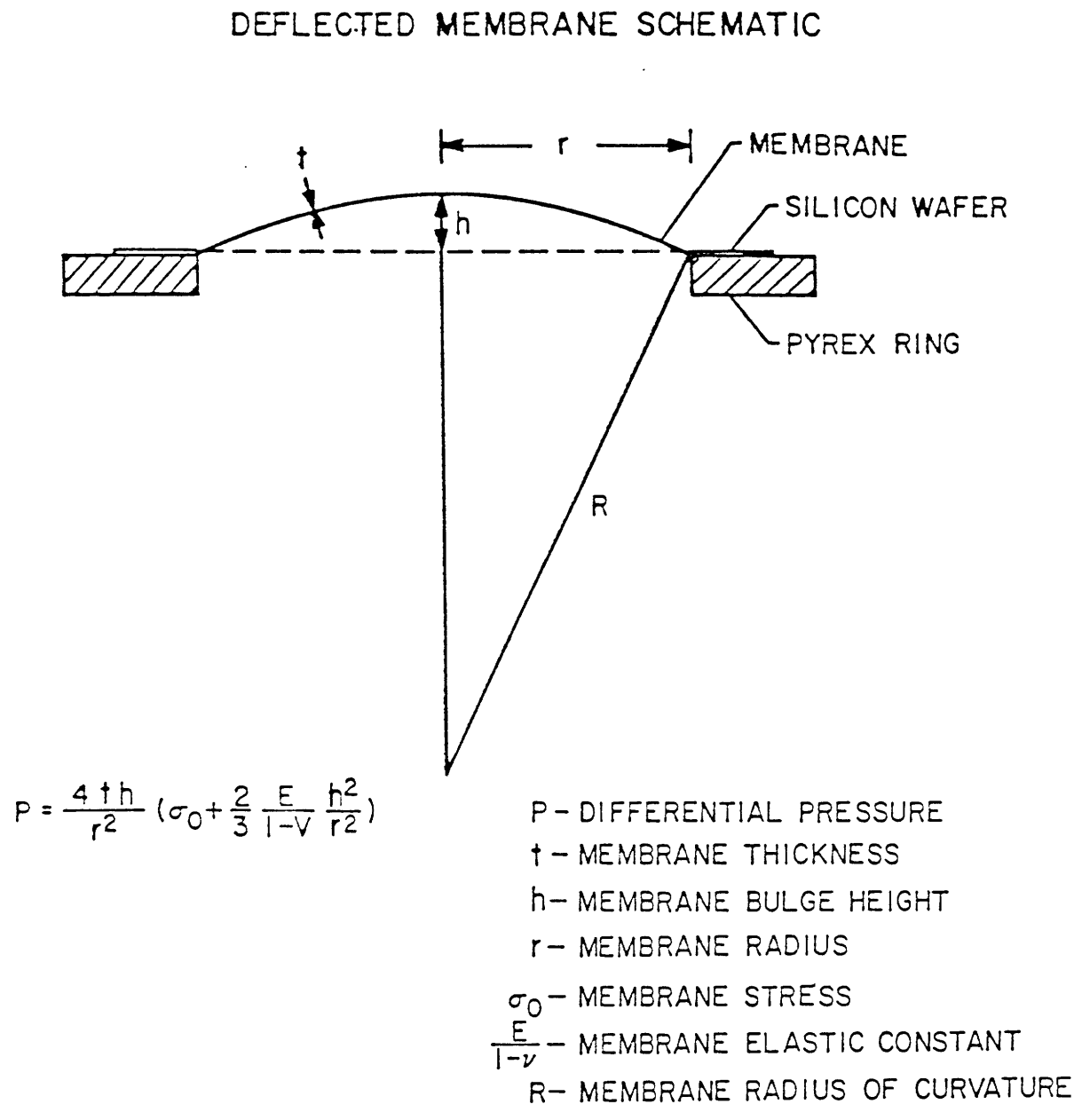

Figure 4. Deflected membrane schematic.

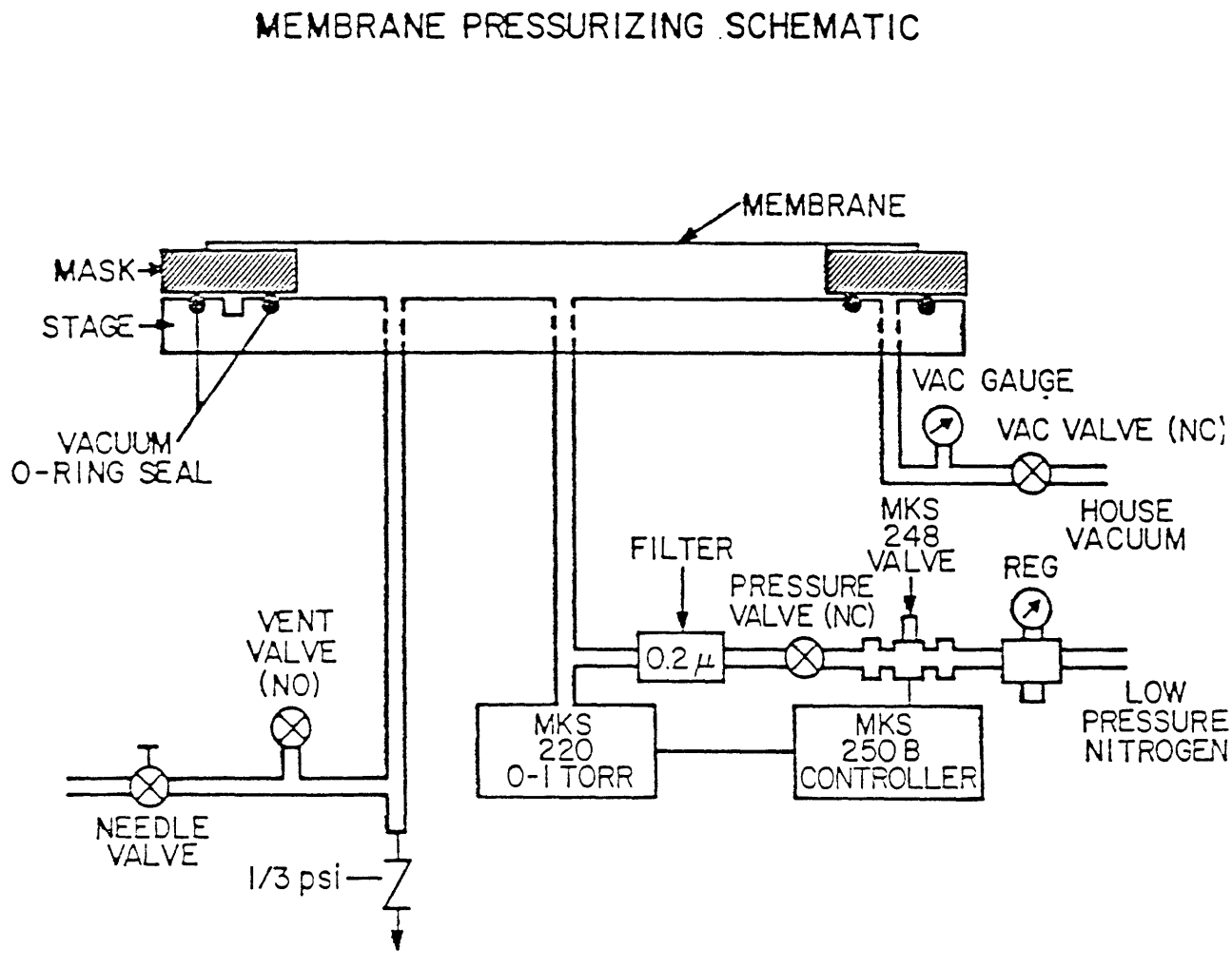

Figure 5. Bulge test setup.

off several mirrors and finally delivered to a position sensitive photodetector. The signal from the detector was (after amplification) sent to the Y input of an HP 7035B x-y recorder. As the mask was moved under the laser, the change in the mask contour was measured as a function of distance. The displacement was monitored on the x input of the x-y recorder. For this particular system, it scanned across 40 mm of the membrane diameter. The radius of curvature of the membrane is given by:

$$R = 1180 / Y$$

where R is in meters, and Y is the recorder translation (in millimeters) in the Y direction corresponding to the 40 mm membrane scan. (6)

3.2.3 Optical Transmittance (AT&T)

In order to determine the thickness of the membrane, an optical analyzer scanned the entire spectrum of 400 to 800 nm. A plot of transmittance versus wavelength data is thus obtained. Position and spacing of transmission peaks in optical spectra were used to determine the membrane thickness. The locations of these interference peaks, caused by multiple reflections between membrane surfaces, were fitted according to the formula:

$$m \lambda_l = 2 n(\lambda_l) t$$

where t is membrane thickness, m = 1,2, 3,...λ_l is the wavelength of the transmittance peak l, and $n(\lambda_l)$ is a wavelength dependent refractive index of Si, as determined from ellipsometric measurements. (10)

4. SILICON-RICH LPCVD NITRIDE MEMBRANES

The following work with nitride membranes was done at MIT Submicron Structures Laboratory.

4.1 Formation of low pressure LPCVD Nitride

The mask fabrication procedure is outlined in Figure 6. Fabrication begins by coating the silicon wafers with silicon-rich, low-stress, LPCVD SiN_x. This was done at both Foxboro and U.C. Berkeley. LPCVD is performed at a pressure of 120 mT, a temperature of 800 °C, and a dichlorosilane/ ammonia flow rate ratio of 6:1. A deposition time of 6 hr at a rate of 30 Å/ min. produces a ~ 1 μm thick film with a stress of ~ 2 x 10^9 dynes/ cm^2. Because of the lower pressure as well as the temperature compensation in the LPCVD tube, the stress uniformity should be excellent. (7)

A backside CF_4 reactive ion etch (RIE) step strips the nitride from the back of the wafer. The wafer is then cleaved into quarters, and anodically bonded to an optically-flat Pyrex ring. Another RIE step and a KOH solution etch (to remove the silicon) are subsequently performed. A plasma etch is used because silicon-rich nitride is very difficult to pattern using conventional wet etching. Instead of defining the hole by applying photoresist to the backside of the mask, a machined aluminum stencil is placed over the wafer during RIE. A special RIE target is used, allowing careful placement and alignment of wafers and stencils. Membranes produced in this manner are typically 1-3 cm in diameter.(7)

4.2 Characterization of membranes

The quality of the membranes was evaluated by a variety of experimental measurements. The thickness and thickness uniformity were measured with the alpha step and the "green light test", respectively. The stress was measured with resonant frequency test. The bulge test

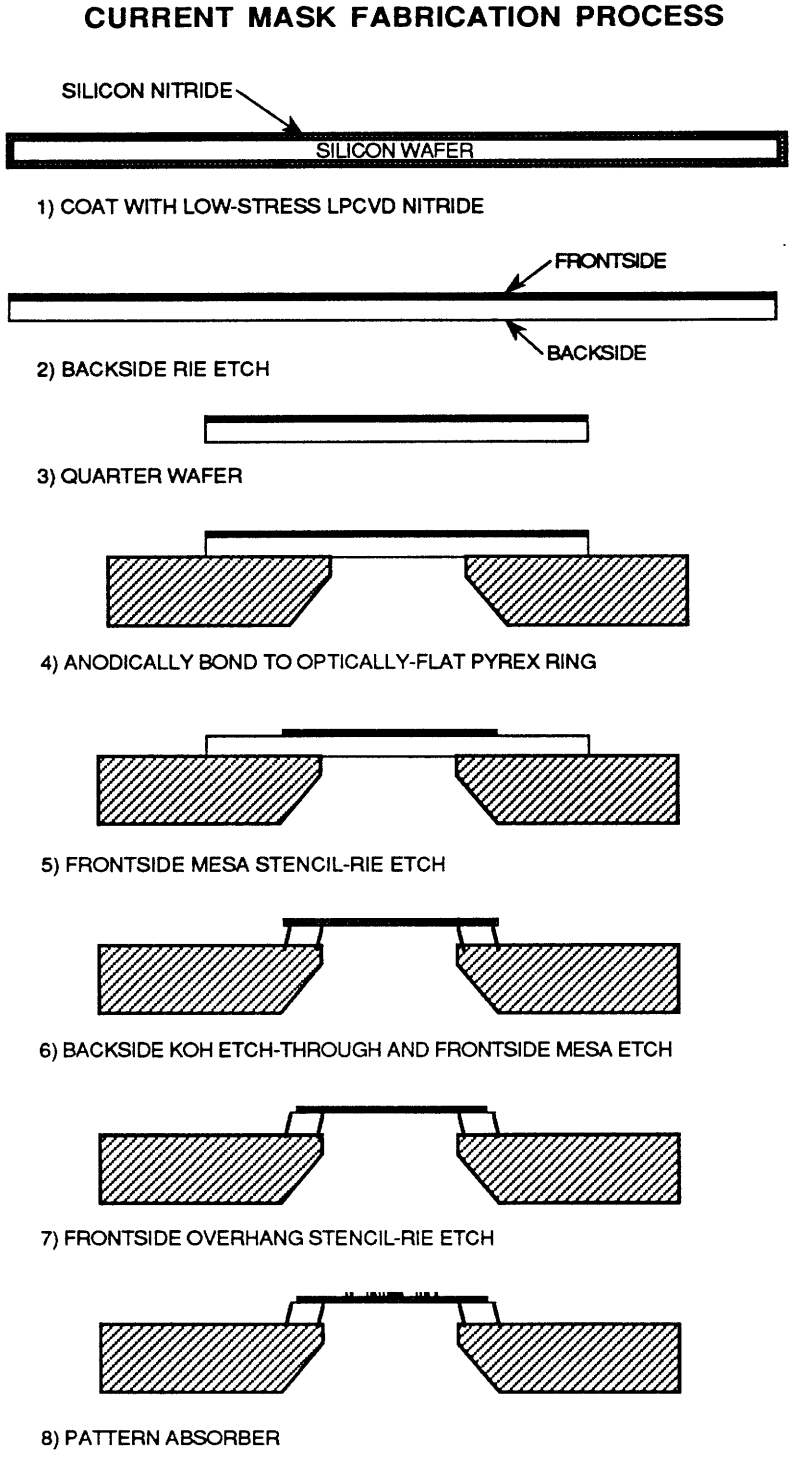

Figure 6. Mask fabrication procedure.

provided another means of determining stress as well as Young's modulus. Using the same apparatus, the burst test was performed on selected wafers to measure membrane strength. A new computerized optical transmission experiment allowed for the unambiguous determination of both thickness and the real and imaginary components of the refractive index.

4.2.1 Green Light and Alpha-Step Test

Measurement of thickness uniformity was done with a Midwest Scientific Unilamp by observing the number of fringes on the wafer when placed under the lamp. For a preliminary measure of thickness, a small piece of membrane was taken from the edge of the mesa after KOH etching, and the average thickness determined from the Tencor Alpha Step 2000.

4.2.2 Resonant Frequency Test

The resonant frequency of the membrane is measured using the set-up shown in Figure 7. The measurement is done at atmospheric pressure and the results are corrected for air loading on the membrane in order to obtain the vacuum resonant frequency ν_{vac}, as shown below:

$$\nu_{vac} = \nu_{air}\left[1 + 1.34\,\frac{a\,d_a}{d_f t_f}\right]^{1/2}$$

where d_a is the density of air, a, t_f, and d_f are the radius, thickness and density of the membrane, respectively. The density of dry air at 20 °C and 760 mm Hg is $d_a = 1.204 \times 10^{-3}$ g/ cm^3. The stress of the membrane can be obtained from:

$$\sigma_o = d_f\,[2.61\,a\,\nu_{vac}]^2$$

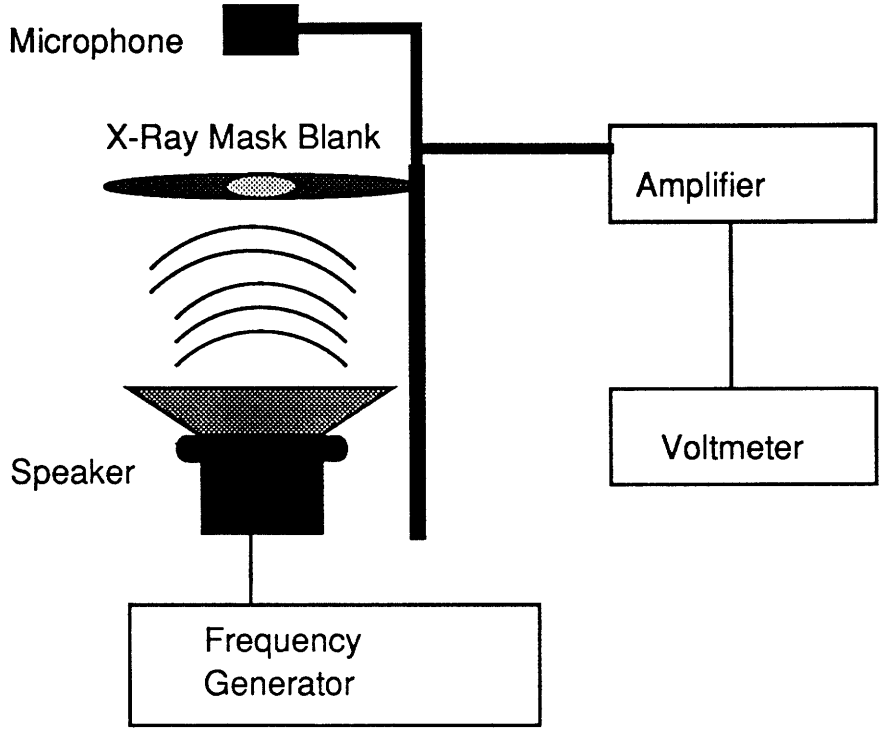

Figure 7. Resonant frequency set-up.

The resonant frequency can be affected by the mounting of the membrane and also by the presence of surfaces which might form a resonant cavity. Ideally a plane wave from the speaker should impinge upon the membrane, exciting an axially symmetric mode of vibration.

4.2.3 Bulge Test (MIT)

As stated previously, the pressure-deflection relationship is determined from the following equation:

$$P = \frac{4th}{r^2}\left(\sigma_o + \frac{2}{3}\frac{E}{1-\nu}\frac{h^2}{r^2}\right)$$

The formula assumes that the bulged film is a hemispherical cap and that it was planar initially under the intrinsic stress σ_o. The value of h is measured with an optical microscope and is determined by subtracting the difference between edge and center deflection. (10)

The bulge test apparatus is depicted in Figure 8. The mask was held in place with an o-ring seal on the wafer. This diagram can be seen in Figure 9. A digital display connected to the optical microscope showed the relative deflection. At each pressure point, two readings were taken to determine the absolute deflection, one at the center and another at the edge of the membrane. Pressure was increased from 0 to approximately 6 psi, and the resulting data points were used to determine the stress and Young's modulus.

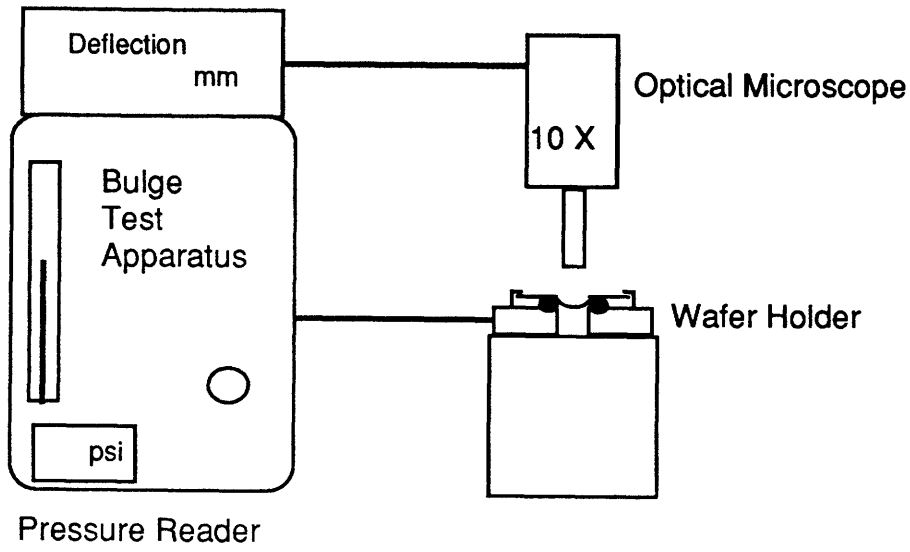

Figure 8. Bulge test set-up.

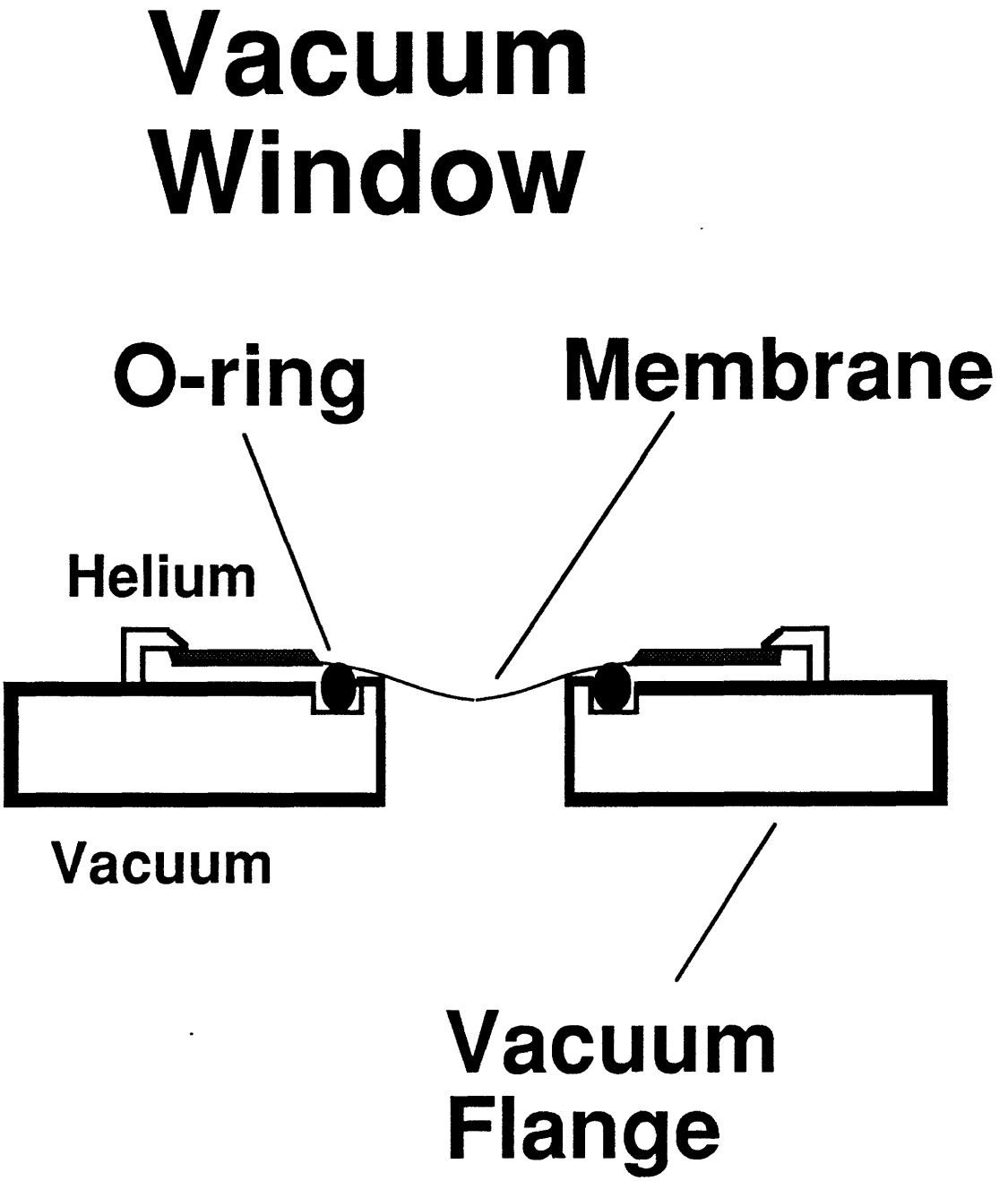

Figure 9. Vacuum window. (Figure provided by Alberto Moel)

4.2.4 Burst Test

The burst test uses the bulge test apparatus, in the mode where the o-ring touches the membrane, and applies pressure until burst and records burst pressure. This pressure determines the Figure of Merit, used for comparing strengths of different membrane materials. The following formula is used for computing the Figure of Merit (FOM):

$$FOM = \frac{P_b (2r)^2}{t\,h}$$

where P_b is the burst pressure, r is the radius of o-ring, t is membrane thickness, and h is maximum deflection (h_{center} - h_{edge}) before breakage.

4.2.5 Optical Transmission Test (MIT)

In order to determine the thickness of the membrane as well as refractive index of the material, an optical analyzer setup, shown in Figure 10, was used. An OSRAM Xenophot HLX bulb with intensity 50 W serves as the light source for the measurements. A regulated DC power supply controls the intensity with minimal fluctuation. The SA Instruments microprocessor scan controller is connected to the H-20 5982 stepper motor, which increases and decreases the wavelength of the H-20 1200 VIS monochromator. This operation is implemented by a Macintosh IIci LabView program connected to the microprocessor. First, a pulse input from the LabView program to the microprocessor increments the monochromator wavelength, then the analog signal acquired from the detector output is collected by the LabView A/D convertor. The graphical block diagram is shown in Figure 11. The digital output and analog input signals were acquired via the Lab-NB Board. In this fashion, the transmission versus wavelength data is graphed on the computer.

Instead of assuming a refractive index from an ellipsometry measurement of the material, as done for the poly-silicon, this value is extracted from the transmission curve from a Nelder-Mead fitting analysis. From the transmission versus wavelength graph, the thickness d and the refractive index $N(\lambda)$ are allowed to vary in order to find the best fit. The following equation was used for the fitting routine:

$$T = \left| \frac{4\,N\,e^{-j\beta}}{(N+1)^2 - (N-1)^2 e^{-2j\beta}} \right|^2$$

which was derived for the case of zero incident angle (i.e.direction of propagation is perfectly normal to the film surface). (1)

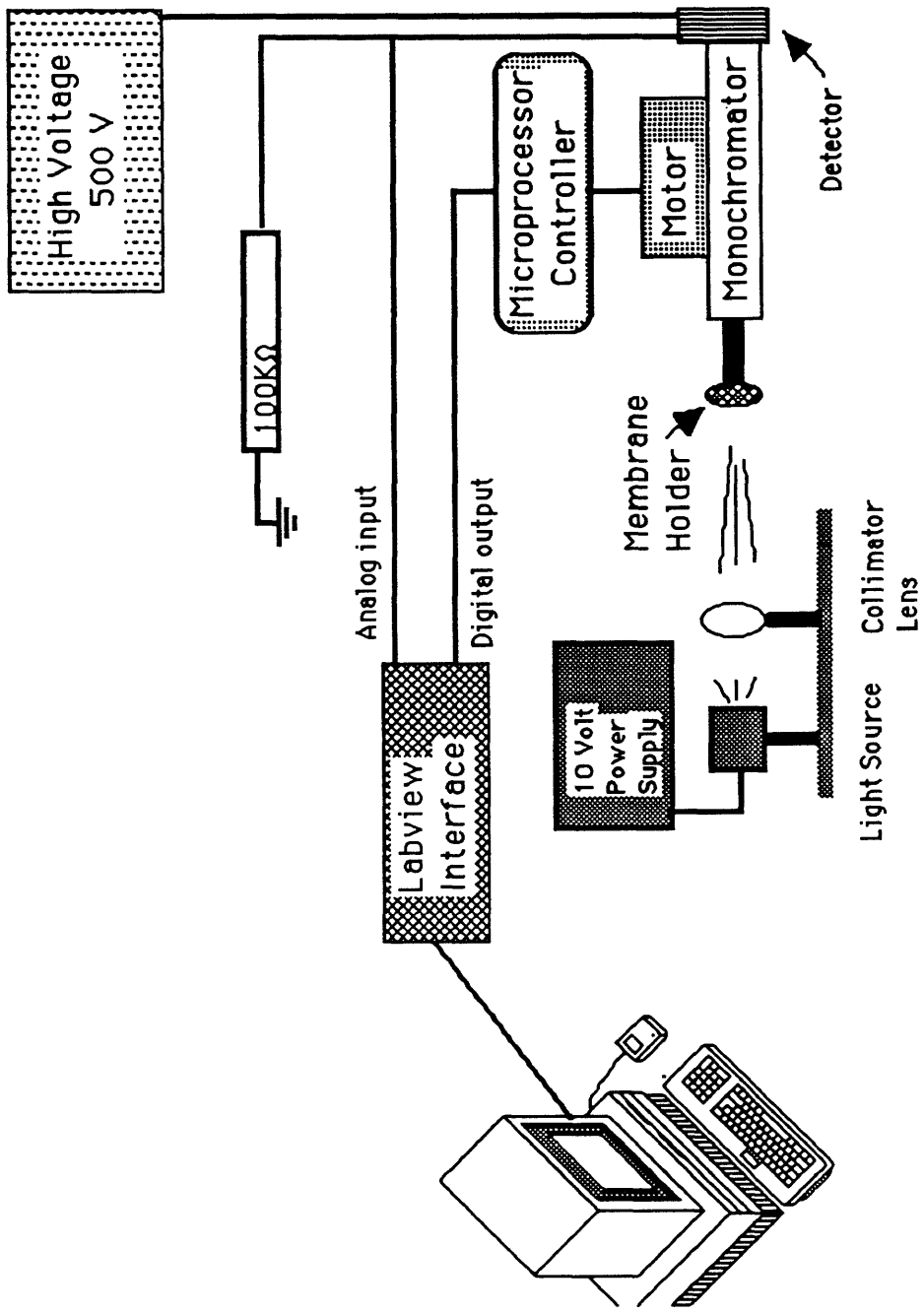

Figure 10. Optical analyzer set-up.

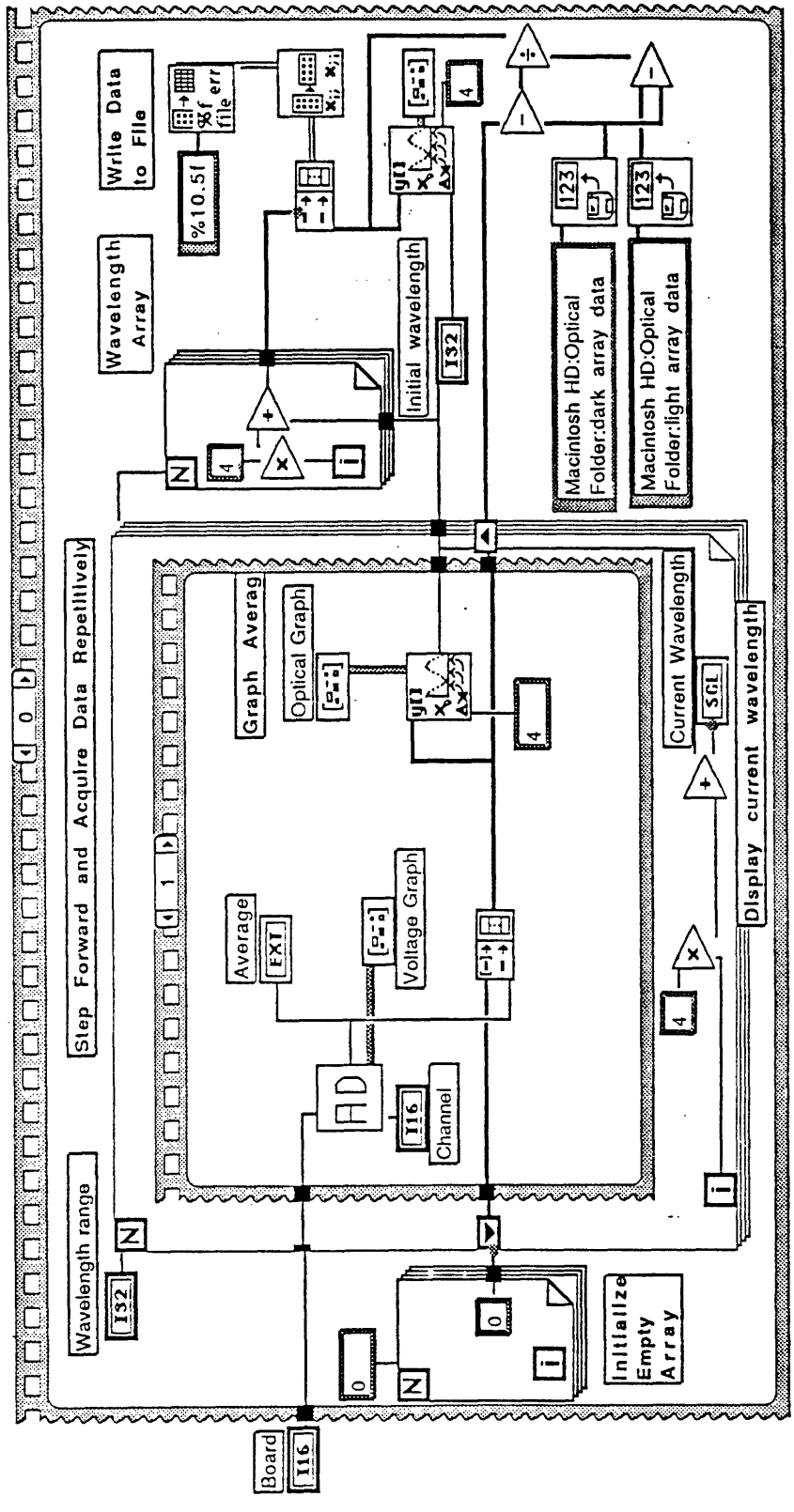

Figure 11. Labview graphical block diagram.

The phase angle ß (film phase thickness) is given by:

$$\beta = \frac{2\,\pi\,d\,N(\lambda)}{\lambda},$$

where $N(\lambda)$, consisting of both the real and imaginary parts of the the refractive index, is given by:

$$N(\lambda) = n(\lambda) - j\,k(\lambda) \qquad (4)$$

and the form of the real part of the refractive index is defined as:

$$n(\lambda) = n_0 + \frac{n_2}{\lambda^2} + \frac{n_4}{\lambda^4}$$

and the imaginary terms are:

$$k(\lambda) = k_0 + \frac{k_1}{\lambda} + \frac{k_3}{\lambda^3}$$

A Matlab function, FMINS, implemented the Nelder-Mead simplex algorithm to find the minimum of a function of several variables (nonlinear optimization). The fitting routine returned a best fit for d, n_0, n_2, n_4, k_0, k_1, and k_3. Figure 12 shows the Nelder-Mead fitting algorithm used in the program, which first sets up a simplex near the initial guess, then iterates until the diameter of the simplex is less than the stopping tolerance.

```
function [x, cnt] =
fmins(funfcn,x,tol,prnt)
% C. Moler, 8-19-86
% Copyright (c) 1986-88 by MathWorks.

[n,m] = size (x);
if  m > n
 x = x';
 n = m;
end;
if nargin < 3, tol = 1.e-3; end
if nargin < 4, prnt = 0; end
cnt = 0

%Set up simplex near the initial guess.
v = 0.9*x;
f = feval (funfcn, v);
for j = 1:n
 y=x;
 if y(j) ~= 0
  y(j) = 1.1*y(j);
 else
  y(j) = 0.1;
 end
  v = [v y];
  f = [f feval (funfcn, y)];
end
[f, j] = sort(f);
v = v(:,j);
```

```
if prnt
 clc
 format compact
 format short e
 home
 cnt
 disp(' ')
 v
 f
end

%Iterate until the diameter of the
%simplex is less than tol.
while 1
 test = 0
 for j = 2:n+1, test =
  max(test, norm(v(:,j)-v(:,1),1)); end
 if test <= tol, break, end
 [v,f,how] = fminstep (funfcn,v,f);
 cnt = cnt + 1;
 if prnt
 home
 cnt
 disp(how)
 disp(' ')
 v
 f
 test
end
end
x = v(:,1);
if prnt, format, end
```

Figure 12. Nelder Mead simplex algorithm.

5. RESULTS AND ANALYSIS

5.1 POLY-SI MEMBRANES ON SILICATE GLASSES

The following work with poly-Si membranes was done at AT&T Bell Laboratories in Murray Hill, NJ.

5.1.1 Light Scattering Test (AT&T)

Table 1 summarizes the light scattering data obtained from poly-Si membranes. The data for epi-Si and diamond are also shown for comparison. Measurements were taken from both the frontside and backside of the membrane, where frontside is defined as the non-etched side of the wafer facing the laser source. Therefore, the frontside should generally be smoother and have less surface scattering than the backside.

Table 1. Light scattering measurements.

	FRONTSIDE			BACKSIDE			%transmit
membrane	B/D 10^{-4}	F/D 10^{-4}	F/M 10^{-4}	B/D 10^{-4}	F/D 10^{-4}	F/M 10^{-4}	M/D 10^{2}
Poly2 Le	1.38	0	0	1.47	.129	.43	30.0
Poly2 Si	.9	0	0	1.01	.194	.645	30.0
Epi-Si	.9	.71	1.9	1.1	.303	.81	37.4
Diamond	122	71	119	21	169	283	60.0

F = forward scattered light

B = backscattered light

D = direct light on photodetector

M = direct light through membrane

where T, B, D, and M are all measured voltages from the two photodetectors. Measurements were normalized for the individual detectors, and each recorded point represents the average of several measurements. Whenever the measurement was comparable to the background noise level, it appears as zero in the table.

As seen from the data, both poly-silicon and epi-silicon had negligible scattering effects. The little difference between these membranes can be attributed to noise. The diamond membrane, however, showed significantly higher scattering. This is due to the rougher surface as well as larger grain size of diamond, the two important causes of scattering. The forward scattering is insignificant, in the case with poly and epi-silicon; however, there is always some nonnegligible backscatter observed. Surface roughness is probably the cause of most of the backscatter, although the little backscattering that is measured can easily be ignored due to its size. The forward scattering, however, is more likely to be determined by the bulk properties of the material such as grain boundaries. (11) Therefore, the surface roughness and the grain boundaries of the poly-silicon membranes are not enough to cause much scattering, indicating that the poly-silicon membranes possess very smooth surfaces that do not scatter significant amounts of light. From the optical alignment point of view, this is a large advantage of poly-silicon over diamond, a material of higher transparency but greater surface roughness. However, in order to determine the suitability of the x-ray mask material, one must take into account other factors such as distortion, strength, and stress.

5.1.2 Stress (Bulge) Test (AT&T)

24 poly-silicon membranes on LE glass were analyzed for stress and Young's modulus. A graph of a sample membrane is shown in Figure 13. Also, a compiled plot of the stress of all 24 membranes can be seen in Figure 14. Average stress of the 24 membranes is 2.15×10^9 dynes/cm^2. Average Young's modulus is 2.4×10^{12} dynes/cm^2. The stress variation among the membranes were on the order of $\pm 10\%$.

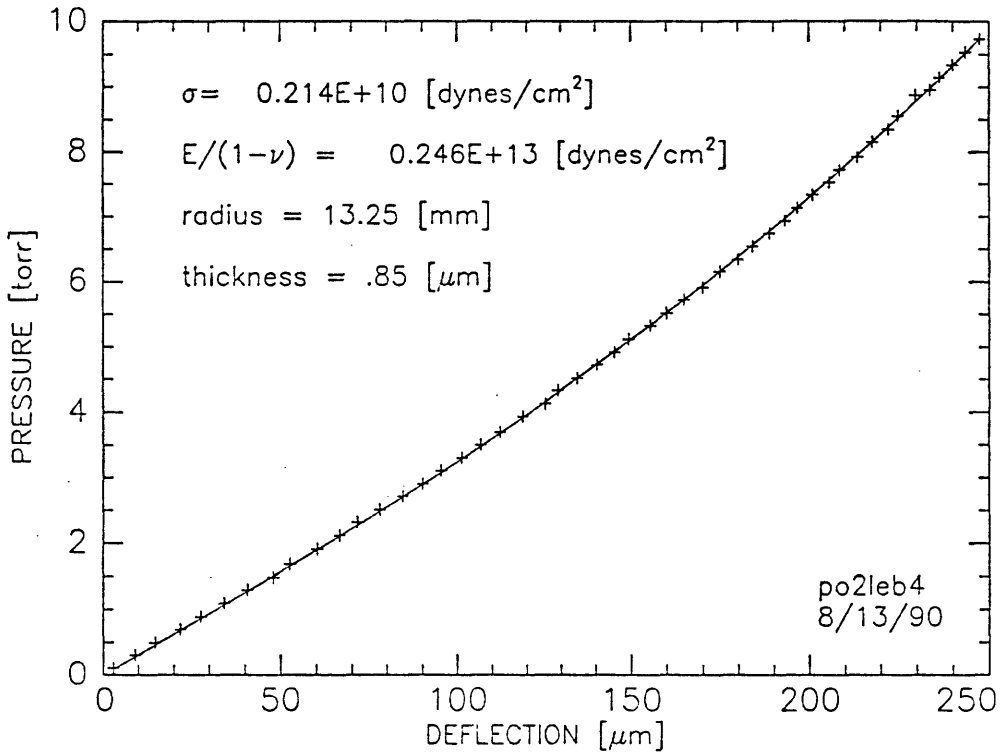

Figure 13. Pressure vs. deflection curve for polysilicon membrane.

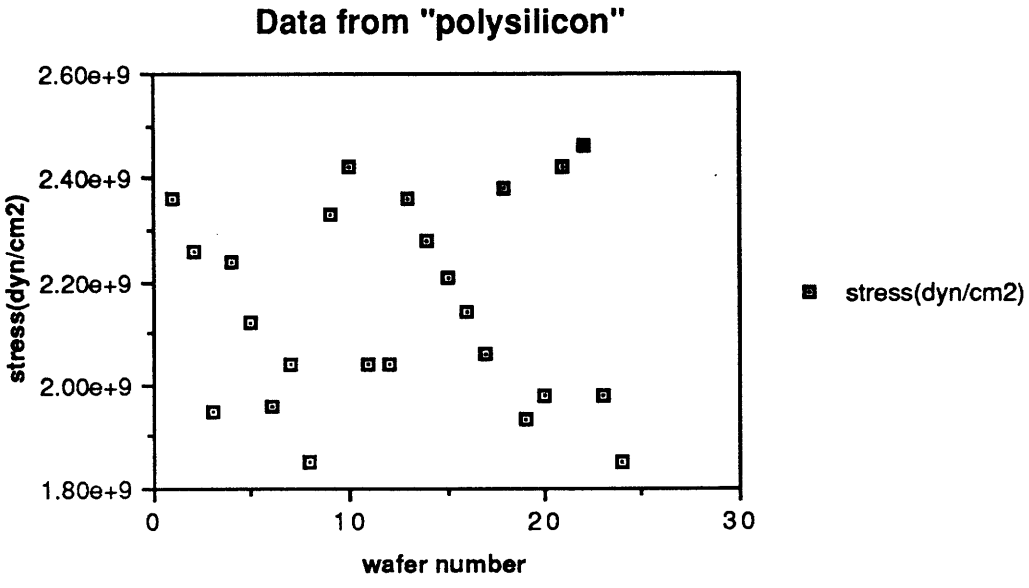

Figure 14. Stress data on 24 polysilicon membranes.

5.1.3 Optical Transmission Test (AT&T)

The same 24 membranes were analyzed for thickness using the optical transmission test. Figure 15 shows the transmission vs. wavelength curve for a sample membrane. A least squares fitting routine was used to determine the thickness. The thickness data for all 24 membranes is presented in Figure 16. The difference in thicknesses is attributed to the two process runs, one producing thicknesses of about 0.85 μm and the other resulting in thicknesses of around 0.7 μm. Because the wafer numbers were not sorted according to the specific process run, a discrepancy in thickness is observed. However, once the wafers are separated by the process involved, one can observe the deviation in thickness is ±1.5% and ±4% for the 0.85 and 0.7 μm wafers, respectively.

5.2 SILICON-RICH LPCVD NITRIDE MEMBRANES

The following work with nitride membranes was done at MIT Submicron Structures Laboratory.

5.2.1 Green Light and Alpha-Step Test

Excellent uniformity was observed for the wafers using the green light test. Variation was on the order of half a fringe throughout the wafer surface. The graph of the thickness of a sample membrane is shown in Figure 17. Figure 18 shows the thickness of selected wafers from Foxboro, numbered 1-20, used in the experiments, where wafer position refers to the position of the wafer in the boat in which they were given. Typical variation was less than 2%.

5.2.2 Resonant Frequency Test

Figure 19 shows the graph of the resonant frequency measured for the membranes. The corresponding stress value is shown on the right axis. Average stress of membranes is 1.32 x 10^9 dynes/cm^2. The stress variation among the membranes were on the order of ±3%.

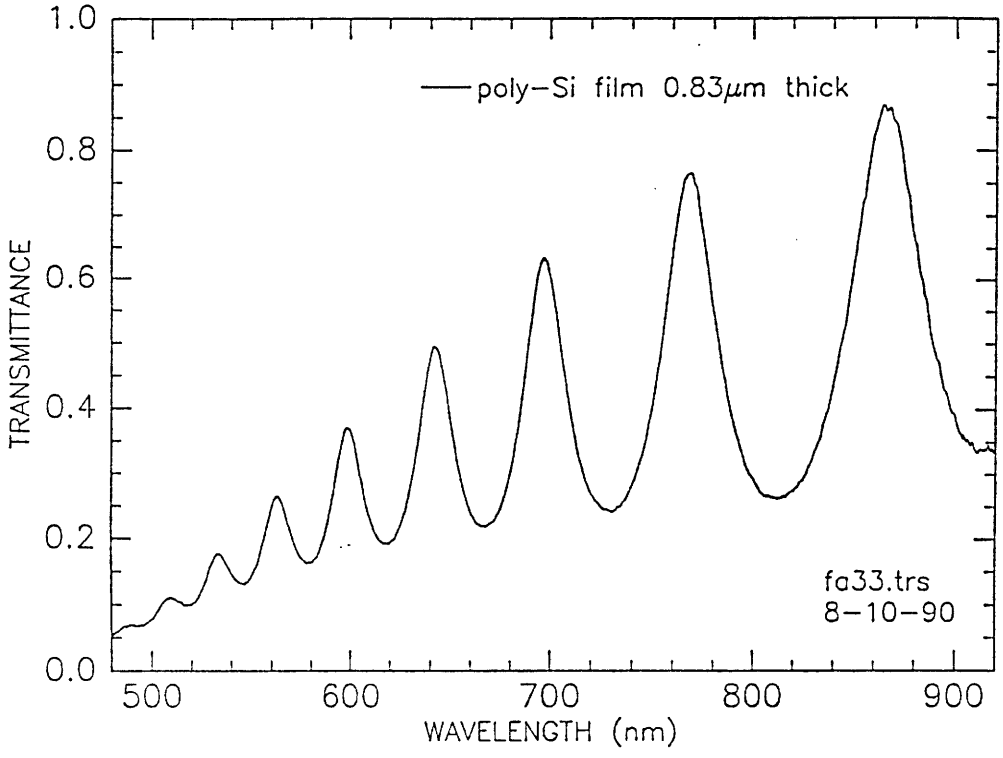

Figure 15. Optical transmission curve for polysilicon membrane.

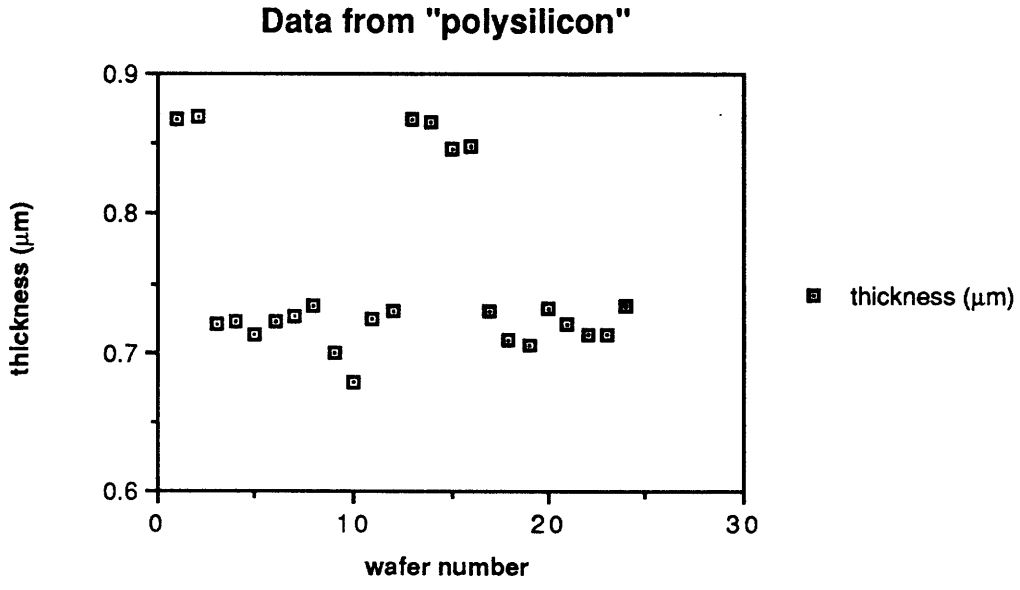

Figure 16. Thickness data on 24 polysilicon membranes.

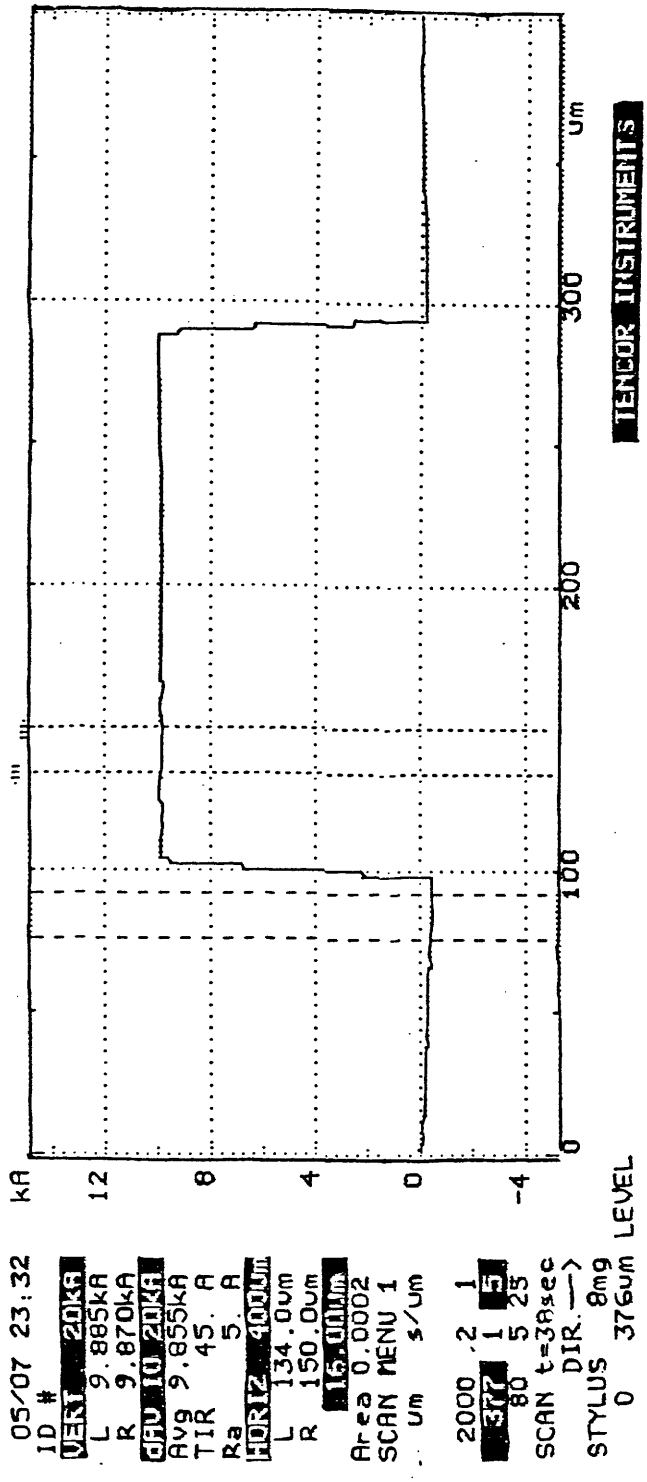

Figure 17. Alpha step thickness profile for silicon nitride membrane.

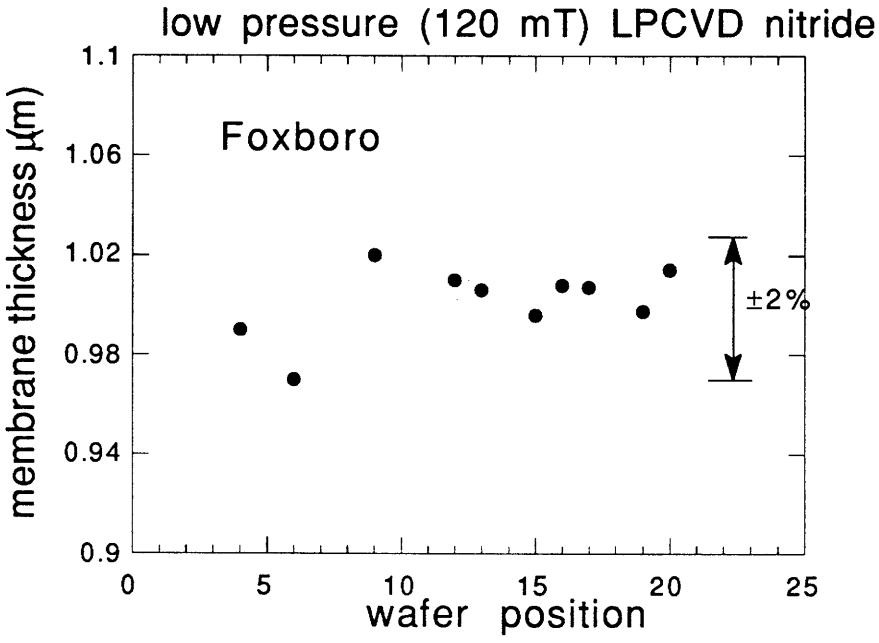

Figure 18. Graph of thickness variation for silicon nitride membranes.

(Figure provided by Yao-Ching Ku)

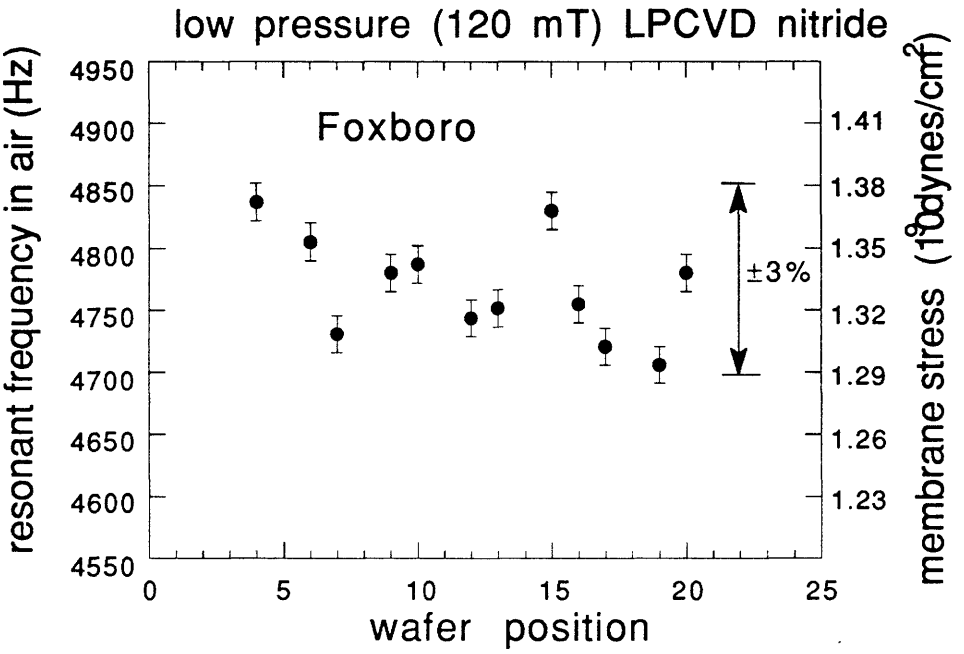

Figure 19. Resonant frequency summary data.

Compared to the poly-silicon membranes, the stress of the silicon nitride was slightly lower. The nitride exhibited lower variation also, but only 12 membranes were analyzed, as opposed to 24 for the poly-silicon. As wafer position increased (going towards the back of the boat), a general tendency towards decreased stress can be observed. The probable cause of this is the deposition condition, where temperature was increased from 793 to 807 °C from the front to the back of the LPCVD tube to compensate for gas depletion. Depending on the air correction factor, the resonant frequency method can be an extremely accurate way to determine stress without bulging the membrane.

5.2.3 Bulge Test (MIT)

A plot of pressure vs. deflection for a sample silicon nitride membrane is shown in Figure 20. Figure 21 shows the measurements on four different wafers loaded at positions 4, 6, 9, and 12 in the "boat" in which they were given. The data reveals variations among membranes from the same wafer, as well as little correlation with the resonant frequency measurements. Many factors can account for these deviations. The bulge test was operated manually, both in increasing the pressure and determining the deflection value. A large part of the error may result from readings that were slightly off the center of the membrane, resulting in different stress values. Another element to consider is that the membrane focusing may not be exact. As deflection increases, focusing on the membrane becomes increasingly difficult, which could possibly lead to recording incorrect values of deflection. Yet another consideration is the control of pressure by the operator. The stress is determined by the linear portion of the curve, which is defined by the first few points. The polysilicon membranes were exposed to a pressure differential up to 10 torr, equivalent to 0.19 psi. The pressure increments for the nitride were approximately 0.1 psi, which may be too large an interval for an accurate fitting. Thus, too few points were taken near the beginning because of the limitations of the pressure controller. The disadvantages of this particular bulge test setup should result in more emphasis on the resonant frequency data, which may be more reliable.

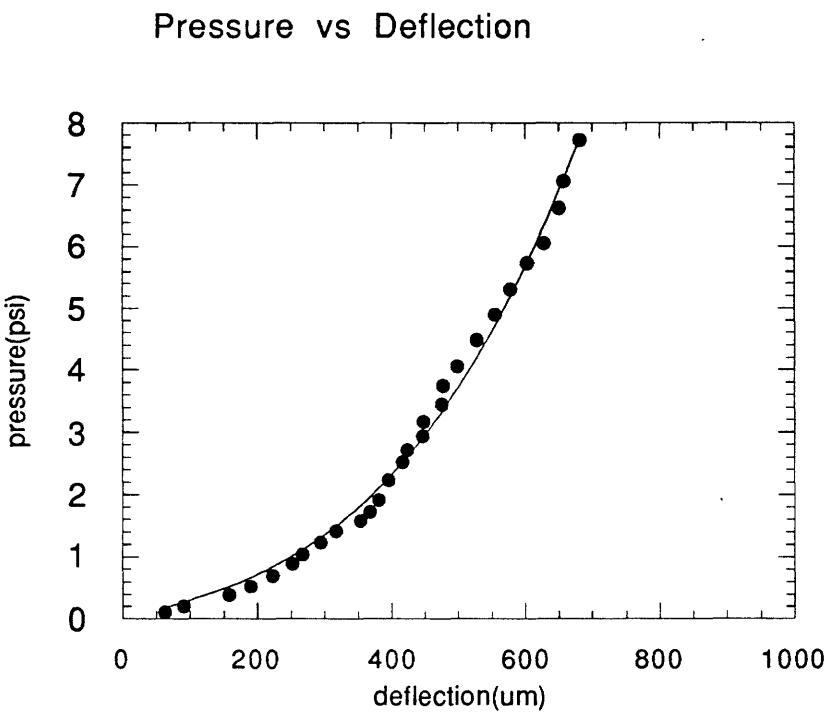

Figure 20. Pressure vs. deflection curve for sample nitride membrane.

(Figure provided by Yao-Ching Ku)

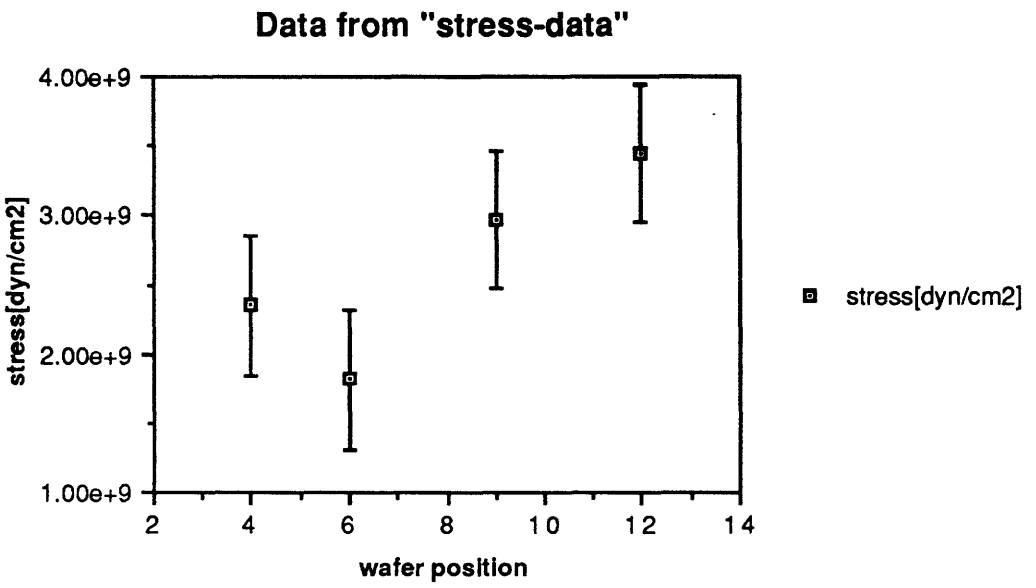

Figure 21. Stress summary data.

5.2.4 Burst Test

Table 2 shows the summary of the burst pressures of selected membranes.

Table 2. Burst pressure data for silicon nitride membranes.

Wafer position	P_{burst} [psi]	h_{max} [μm]	FOM [atm]	Diameter o-ring
7	9	148	4.06×10^5	1 cm
10	26	324	5.36×10^5	1 cm
12	>54 (did not break)			1 cm
13	41	421	6.59×10^5	1 cm
16	45	422	7.20×10^5	1 cm
17	31	347	6.04×10^5	1 cm
19	14	229	4.17×10^5	1 cm
20	23	346	4.46×10^5	1 cm

The burst pressure was extremely high for most membranes, especially near the center of the boat. Membrane 12 did not break even at the maximum pressure (~ 60 psi). This indicates that the membranes are very strong and durable. Because a similar experiment was not performed on the poly-silicon membranes, no comparison can be made between the two materials.

Some sources of error in calculating the FOM result from determination of thickness and maximum deflection. The alpha-step measurement was used for the membrane thickness, which may result in some error if there is a gap (i.e. membrane was broken and a fragment measured in Alpha Step) between the membrane and the substrate it is on. The maximum deflection was determined by subtracting the edge from the center deflection. Sometimes, the edge deflection could not be read above 10 psi because the membrane became too dark to focus properly, so this value was extrapolated from the previous deflection values.

5.2.5 Optical Transmission Test (MIT)

Figure 22 shows the optical transmission vs. wavelength curve and the fitting curve for a silicon nitride membrane. The real and imaginary components of the refractive index as well as the thicknesses are shown in Table 3.

Table 3. Summary of refractive index data.

wafer position	d [nm]	n @633nm	k @633nm	d(alpha-step) [nm]
7	931.8	2.3058	0.0034037	1020
9	932	2.3077	0.0033698	1020
13	934.8	2.3025	0.0029627	1006
15	930.6	2.3143	0.0036254	996
17	918.7	2.3143	0.0035904	1007
19	928.9	2.3113	0.0038924	997.5
20	921.9	2.3064	0.0033587	1014

The thicknesses determined by the optical method were very uniform overall, with a variation of ±0.87%, but were thinner than those determined by the alpha-step method. The real refractive index of ~ 2.3 is slightly higher than the value of 2.2 reported by Foxboro from ellipsometry measurements. Many factors can account for these discrepancies. First of all, the alpha-step method of determining thickness is not perfect. As mentioned earlier, a bad membrane to wafer contact may result in inaccurate readings. Also, the wavelength-dependant refractive index equation is simplified, and including additional higher order terms may produce more reliable results. A graph of the real and imaginary refractive indices versus wavelength can be seen in Figures 23 and 24, respectively. The real refractive index graph agrees fairly well with theory, but the imaginary index increases slightly after about 625 nm. As indicated earlier, adding higher order terms to the imaginary refractive index equation could possibly correct this error. Overall, the optical experiment shows great promise in determining the refractive index and thickness with high accuracy, which has not been achieved before.

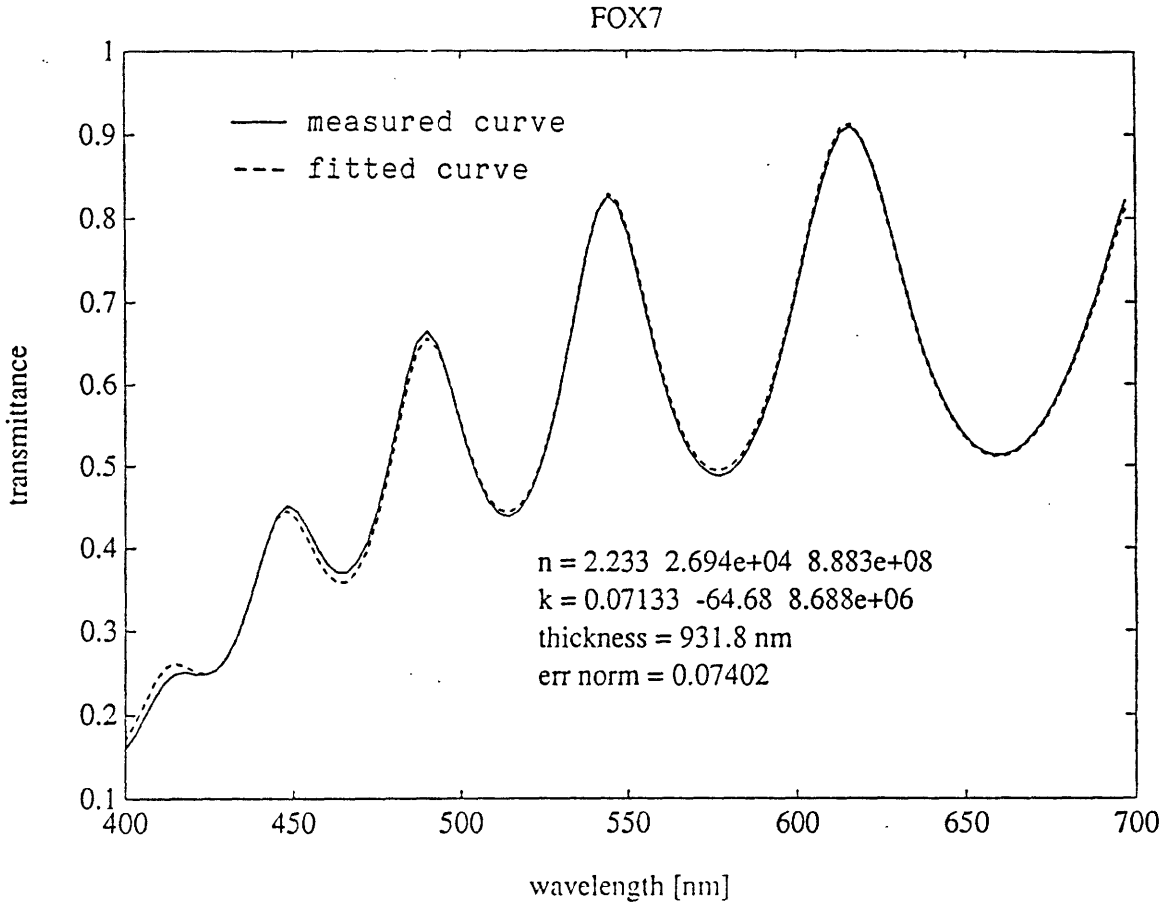

Figure 22. Optical transmission curve for nitride membrane.

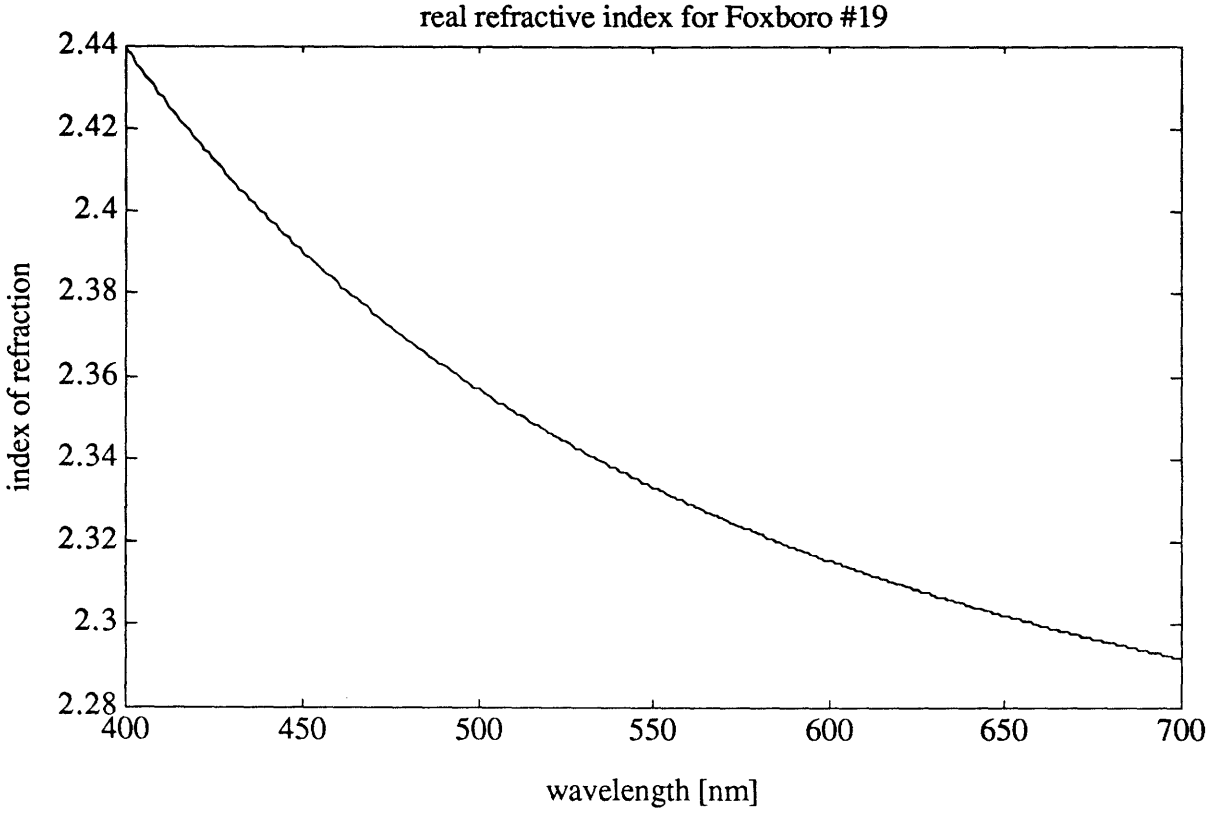

Figure 23. Graph of real refractive index vs. wavelength.

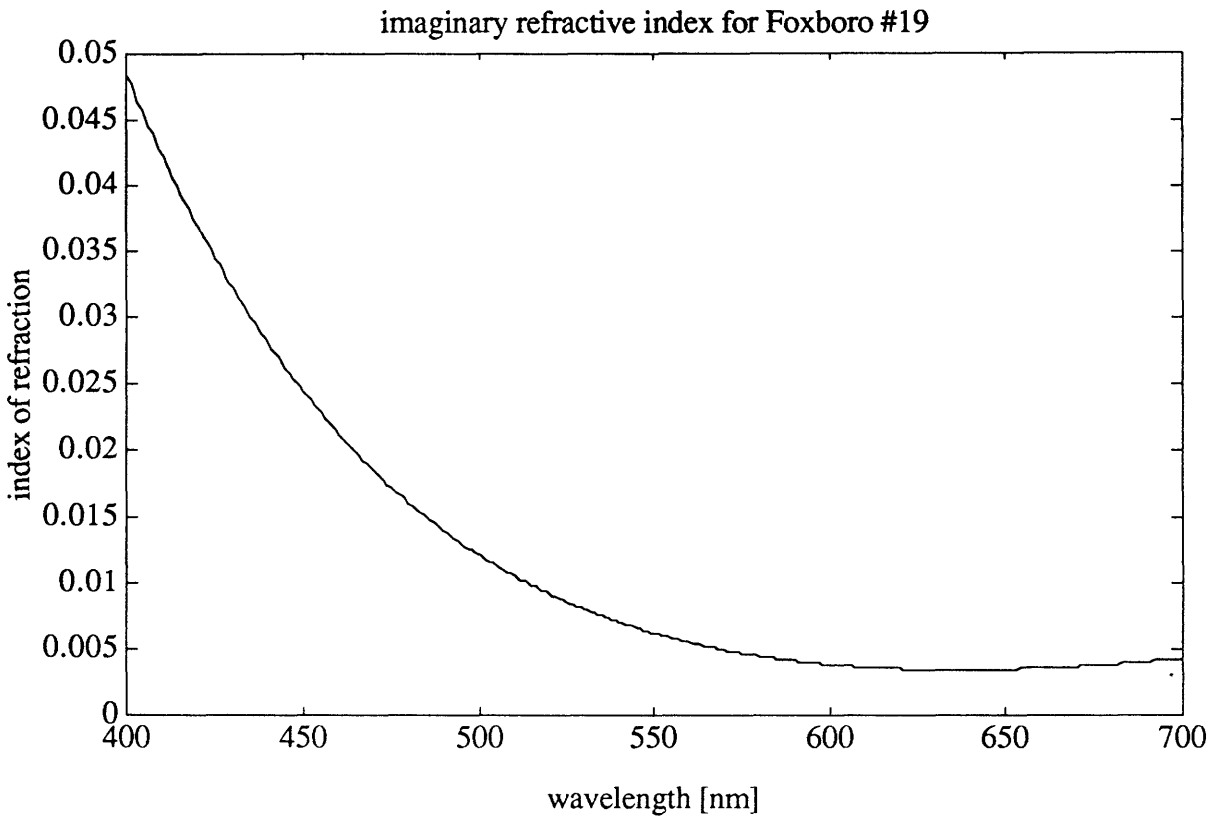

Figure 24. Graph of imaginary refractive index vs. wavelength.

6. CONCLUSIONS

The results of the characterization measurements indicate the feasibility of using both Si-nitride and poly-Si as x-ray mask materials. Advantages of Si-nitride include high breaking strength, high optical transparency, and low stress. Advantages of poly-Si include low scattering, as well as high optical transparency and low stress.

Si-nitride exhibited slightly lower stress than poly-Si (average of 1.32×10^9 versus 2.15×10^9 dynes/cm^2). For the nitride, the resonant frequency method proved a more effective way of determining stress. The poly-Si bulge test setup was also extremely reliable because of the automated system used. However, the stress values measured are still rather high to use in an x-ray mask system. Realistically, stress on the order of $6 - 8 \times 10^8$ dynes/cm^2 will be required for a material in order to minimize distortion as well as maximize flatness. Thus, future processing adjustments leading to lower stress should be made.

The new optical experiment was very successful in determining thickness as well as the imaginary and real refractive indices for the si-nitride. The interference peak method used for the poly-si was simpler, but determined only the thickness of the material, having assumed a previously calculated value of the real refractive index.

An important factor to consider is that the measurement systems differed for the two materials, and some experiments were not performed on both materials, so no comparison can be made. The new light scattering setup demonstrated an efficient way to measure both forward and backward scattering, but the negligible scattering of the poly-si shows that scattering is not a problem in optical alignment for this material. The high burst strength of the nitride indicates extreme robustness and durability for this material.

The experimental process suggest means for improvement of the measurement systems. The accuracy of the MIT bulge test setup can be improved by automating the system, as in the Bell Labs AROC system. The MIT optical system can be sped up so that measurement can scan the entire wavelength instead of incrementing by step. Also, a more efficient fitting algorithm such as the adaptive method should be implemented to speed up the fitting process.

The characterization methods described in this paper are all very important in analyzing the material for x-ray mask fabrication. Depending on whether the emphasis is placed on optical alignment or robustness, either poly-si or si-nitride, respectively, can be deemed superior. In practice, both criteria are significant. Therefore, both materials are excellent choices for formation of x-ray masks, pending improvements in the stress values.

The future course of x-ray lithography will depend strongly on the progress made in the next few years. If the current trend towards smaller linewidth continues, we will reach a limit of optical lithography around the year 2005. For x-ray lithography to become the next generation lithography tool, it will soon have to prove its superiority over optical, e-beam and other types of lithography in terms of cost, resolution, and practicality. X-ray mask substrate and absorber materials need to be standardized for widespread industrial use in the near future. Judging from the data collected in this thesis, I feel that we should emphasize finding a material of lower stress, since optical transmission at high wavelengths does not seem to be a problem in the materials evaluated. Although the stress values for both materials were fairly low, we would require half an order of magnitude lower for practical use in x-ray lithography. Therefore, for x-ray lithography to remain a strong contender, one of two things will have to happen in x-ray mask membrane research. Either changes in processing that result in lower

stress for poly-silicon or nitride will be made, or improvements in another material, such as lowering the roughness of diamond, should be researched. Either way, if favorable trends continue, x-ray lithography should become fully implemented by the beginning of the 21th century.

7. REFERENCES

1. Azzan, R.M. and N. M. Bashara. Ellipsometry and Polarized Light. North Holland Publishing: New York, NY, 1977.

2. Brodie, Ivor and Julius J. Muray. The Physics of Microfabrication. Plenum Press: New York, NY, 1982.

3. Chu, W., A. Yen, K. Ismail, M. Shepard, H. Lezec, C. Musil, J. Meingailis, Y.C. Ku, J. Carter, and H. Smith, "Sub-100 nm X-Ray Mask Technology Using Focused-Ion-Beam Lithography", J. Vac. Sci. Technol. B 7, 1583-1585, Nov/Dec. 1989.

4. Ferrieu, F. and J. H. Lecat, "Spectroscopic Ellipsometry for the Characterization of Thin Films", J. Electrochem. Soc., Vol. 137, No. 7, July 1990.

5. Maldonado, J.R., "X-Ray Lithography, Where It Is Now, and Where It Is Going", Sept 1989.

6. Resnick, D.J. and W.M. Mansfield, "Stress Determination of X-ray Mask Membrane", July 1985.

7. Schattenburg, M.K., K. Early, Y.C. Ku, W. Chu, M.I. Shepard, S.C. The, and H.I. Smith, "Fabrication and testing of 0.1 μm linewidth microgap x-ray masks", J. Vac. Sci. Technol. B 8, 1604-1608, Nov/Dec. 1990.

8. Spears, D.L., and H.I. Smith, "X-Ray Lithography - A New High Resolution Replication Process", Solid State Technol. 15, No. 7, 21-26, 1972.

9. Trimble, L.E., G.K. Celler, and J. Frackoviak, "Control of Optical and Mechanical Properties of Polycrystalline Silicon Membranes for X-Ray Masks", SPIE Vol 1263, p.251, 1990.

10. Trimble, L.E., and G.K. Celler, "Evaluation of Polycrystalline Silicon Membranes on Fused Silica for X-Ray Lithography Masks", J. Vac. Sci. Technol. B 7, p. 1675, Nov/Dec. 1989.

11. Vladimirsky, Y., et al, "Optical Properties of X-Ray Lithography Masks", EIPB Conference, May/June 1990.

12. Warlaumont, J., "X-Ray Lithography: On the Path to Manufacturing", J. Vac. Sci. Technol. B 7, Nov/Dec. 1989.

13. Wilson, Alan D., "X-Ray Lithography: Can it Be Justified?", Solid State Technol., p. 249-255, 1986